

Numerical Investigation of Multiphase Flow through Complex Fractures

Prakash Purswani^{1,*}, Javier E. Santos¹, Jeffrey D. Hyman¹, and Eric J. Guiltinan¹

¹Earth and Environmental Sciences Division, Los Alamos National Laboratory, Los Alamos, NM, 87545

*Corresponding author: Prakash Purswani, ppurswani@lanl.gov

Abstract

Multiphase flow through fractures has great significance in subsurface energy recovery and gas storage applications. Different fracture and flow properties affect flow through a fracture which is difficult to control in laboratory experiments. Here, we perform lattice Boltzmann simulations in an ensemble of synthetically generated fractures. Drainage simulations are performed at different capillary numbers, wettability, and viscosity ratios. We track the invading front and quantify breakthrough saturations and show that roughness and wettability have a profound effect on fluid invasion through a complex fracture. Invading a more viscous fluid results in more stable displacement regardless of the capillary number while at very low capillary numbers, fluid migration is dependent on the inherent structure of the fracture. Through a systematic investigation, we develop fluid displacement phase diagrams across multiple fractures, and demonstrate the importance of natural fracture features of roughness and wettability in establishing stable versus unstable displacement during multiphase flow.

Plain-level Summary—

In this research, we perform multiphase flow simulations through single fractures. We assess the movement of the invading fluid by varying different physical attributes of the fractured media as well as by varying the different fluid flow conditions. Through numerical simulations, we establish strict control on these attributes such that their impact on flow dynamics can be studied independently which is not possible through experiments. Fluid invasion is studied through quantitative metric of fluid invasion front and breakthrough saturations. We show that the dynamics of fluid movement through fractured media is highly sensitive to fracture properties of surface roughness as well as to the flow properties of capillary numbers, wettability, and viscosity ratios.

Keywords— Multiphase flow, fluid flow through fractures, Lattice Boltzmann simulations, surface roughness, wettability, capillary number, viscosity ratio

33 Highlights—

- 34 • High-fidelity multiphase flow numerical simulations are performed through single rough-walled fractured
35 media.
- 36 • A variety of fracture and flow parameters are tested including surface roughness, wettability, viscosity
37 ratios, and capillary numbers.
- 38 • Invading phase front and breakthrough saturations are quantified for the different conditions and phase
39 diagram with stable and unstable displacement regimes are plotted.
- 40 • Displacement regimes are analyzed for a variety of different fracture realizations, and it is shown that
41 the displacement regimes are highly sensitive to the inherent fracture properties.

42 1 Introduction

43 Fluid flow through fractures is of great importance for a variety of geoscience applications pertaining to
44 energy and the environment. Energy applications include safe and long-term geologic carbon sequestration,
45 zero-carbon technologies like geologic hydrogen storage, and hydraulic fracturing for hydrocarbon production
46 Khosravi et al. (2014), Wang et al. (2022), March et al. (2018), Hussain et al. (2021) while environmental
47 applications include secure disposal of nuclear waste and remediation of contaminated groundwater Birkholzer
48 et al. (2012), Ghanbarzadeh et al. (2015), Zhou et al. (2023). Fractures are high-conductive pathways that
49 control most of the flow through tight geologic media where matrix porosities and permeabilities are in the ultra-
50 low range. Fractures are complex and highly heterogeneous with variation both at the small- and large-scale.
51 At the small-scale (mm-cm scale) heterogeneity arises due to fracture aperture distributions/mean apertures,
52 surface roughness, and aspect ratios whereas at the large-scale (m-km scale), fracture lengths, connectivity, and
53 the orientation of the connected fracture govern transport Hyman et al. (2015, 2021), Song et al. (2023). The
54 two scales are inherently interlinked where local heterogeneities directly influence transport at the larger scale.
55 In this research, we focus at the small-scale to investigate the impact of various fracture and flow parameters
56 on the dynamics of multiphase fluid flow through single rough-walled complex fractures.

57 Sophisticated experimental techniques such as x-ray microcomputed tomography (μ CT) have enabled digi-
58 tal characterization of fracture properties. Bertels et al. (2001) performed steady-state experiments using x-ray
59 μ CT in a fractured basalt sample to study the impact of fracture aperture distribution (mean aperture of 336
60 μ m) on phase saturations. During flooding, they measured relative permeabilities and capillary pressures and
61 showed that relative permeabilities are not linear for a gas-water system during flow through a rough-walled
62 fracture and that there was significant retention of water (as the wetting phase) in the fracture. Similarly,
63 Karpyn et al. (2007) performed experiments in a single rough-walled fracture in a Berea sandstone to visualize
64 and quantify fluid occupancy using μ CT. Mechanisms of capillary trapping of the nonwetting phase and by-
65 passing flow of the wetting phase were captured through quantitative image analysis. Importance of fracture
66 aperture and presence of local heterogeneity in the rough surface was found to be critical for phase trapping.
67 Chen, Wu, Fang & Hu (2018) performed experiments to study displacement regimes in a single rough-walled
68 fracture for different capillary numbers and viscosity ratios. The experiments were performed for a water/glyc-
69 erol mixture displacing silicone oil where the invading fluid contact angle was $\approx 161^\circ$. They generated a phase
70 diagram by plotting contours for the nonwetting phase breakthrough saturations and found spatial variability

71 of the fracture domain to cause unstable displacement efficiency. They also found that fluid migrated with
72 a stable displacement in the fracture until some variability was reached, after which fingering was observed.
73 Such flow experiments provide valuable insights regarding fracture and flow attributes; however, these are often
74 cumbersome and yield displacement information for a single fracture. Sophisticated numerical techniques are
75 therefore often used to supplement experimental works.

76 Dou et al. (2013) performed lattice Boltzmann method (LBM) simulations in a self-affine fracture to study
77 the effect of wettability on the evolution of fluid-fluid interfacial area during invading phase flow through the
78 fracture. The nonwetting phase was found to flow through larger openings in the fracture. They found a
79 nonlinear trend of fluid-fluid interfacial area with the invasion of the nonwetting phase with a maximum at a
80 water saturation of ≈ 0.2 . Similar trends have been observed for traditional water-wet porous media through
81 experimental Culligan et al. (2004, 2006) and simulation work (Reeves & Celia (1996), Landry et al. (2014),
82 McClure et al. (2018)). Gultinan et al. (2021) also performed LBM simulations in rough-walled synthetic
83 fractures to study CO₂-brine migration through the fracture. They developed an interface tracking approach
84 for estimating relative permeabilities for such a system involving transient flow and found the dynamics of
85 CO₂ migration through the fracture to be significantly impacted by local aperture and wettability variations
86 in the fracture. Other reports have also demonstrated the importance of wettability through a combination
87 of experimental and simulation work and have extended the traditional displacement phase diagram in the
88 capillary number-viscosity ratio-wettability space Zhao et al. (2016), Lan et al. (2020), Primkulov et al. (2019,
89 2021). Similarly, the effect of surface roughness has been shown to be critical to fluid displacement through
90 fracture Chen, Wu, Fang & Hu (2018), Yi et al. (2019), Hu et al. (2019).

91 Overall, in the literature, there is breadth of experimental and numerical works that study multiphase flow
92 through complex fractures. Further, it is established that different fracture attributes as well as flow properties
93 govern fluid flow through complex fractures. However, there is no study that provides a comprehensive analysis
94 where effects of both flow and fracture properties is considered holistically. In this research, we aim to bridge
95 this gap by taking a systematic approach for quantifying the effect of various flow and fracture parameters
96 on the flow of invading fluid through complex rough-walled fractures. We implement state-of-the-art numer-
97 ical fracture generation technique called pySimFrac Gultinan et al. (2023) and direct numerical simulation
98 technique called MF-LBM Chen, Li, Valocchi & Christensen (2018), Chen et al. (2019) to investigate these
99 scenarios and report our findings for different realistic fracture realizations. We first describe these techniques
100 in Section 2 and describe the simulations sets considered. In Section 3, we discuss the results characterizing the
101 dynamics of fluid invasion for different fracture (Hurst exponent and root mean squared (rms) roughness) and
102 flow parameters (capillary numbers and contact angles) and lastly, we describe the effect of these properties in
103 combination with different viscosity ratios.

104 **2 Methodology**

105 **2.1 Description of fracture generation and numerical simulations**

106 We utilized pySimFrac, a new python-based library, to numerically generate realistic single fracture realizations
107 Gultinan et al. (2023). In addition to fracture generation, we utilized extended capabilities within pySimFrac
108 to perform direct numerical multiphase simulations through the fractures. PySimFrac offers two numerical
109 methods for fracture generation, namely, convolution and spectral-based methods. We used the spectral

110 method for generating the fractures. This method is an extension of the Brown method where three inputs are
 111 required to develop a numerical fracture, namely, the rms roughness, mismatch between the fracture surfaces,
 112 and the fractal dimension Brown (1995). The updated spectral method offers additional capabilities such as
 113 the aspect ratio, fracture seed, as well as the correlation length Glover et al. (1998*a,b*, 1999), Ogilvie et al.
 114 (2006). Here, we vary fracture seed, rms roughness, and the Hurst exponent to study the effect of fracture
 115 surface variability on flow. The Hurst exponent is related to the fractal dimension Babadagli et al. (2015) which
 116 is a measure of the surface texture. It ranges between zero and one with larger Hurst exponent relating to
 117 smaller fractal dimension and producing smoother fractures. The rms roughness parameter, however, calibrates
 118 roughness by controlling the standard deviation of the heights of the fracture surfaces. It scales between zero
 119 and infinity with zero referring to a completely smooth surface and has units of length. The mean aperture of
 120 the fractures generated in this study was fixed at 15 lattice units (lus) which would correspond to 3.3 $\mu\text{m}/\text{lu}$
 121 for a fracture with mean aperture of 50 μm commonly observed for natural fractures in Barnett Shale Gale
 122 et al. (2007), Gultinan et al. (2021).

123 For the direct numerical multiphase simulations, we used an LBM code, MF-LBM, developed at the Los
 124 Alamos National Laboratory (LANL) Chen, Li, Valocchi & Christensen (2018), Chen et al. (2019) (<https://github.com/lanl/mf-lbm>). MF-LBM is a highly-parallelized code that allows for faster execution with
 125 GPU-enabled computing resources. The code is developed using the continuum-surface-force combined color-
 126 gradient (CSF-CD) scheme for delineating the two phases Brackbill et al. (1992), Xu et al. (2017). Furthermore,
 127 MF-LBM uses the geometrical wetting model and the multi relaxation time (MRT) framework for simulating
 128 two-phase flow effectively Leclaire et al. (2016, 2017), d’Humières et al. (2002), Akai et al. (2018). It has been
 129 benchmarked against CO_2 displacement experiments conducted in a 2-D heterogeneous micromodel Chen, Li,
 130 Valocchi & Christensen (2018). In MF-LBM we input flow and rock/fluid interaction parameters including
 131 contact angles, capillary numbers, viscosity ratios, and interfacial tension. All simulations were analyzed until
 132 the breakthrough point of the invading phase. The simulations were executed on the Nvidia A100 GPU partition
 133 of the Chicoma supercomputer at LANL (<https://www.lanl.gov/org/ddste/alosc/hpc/index.php>). The
 134 time required to run the simulations depended on different factors including the input capillary number and
 135 how extreme or simple the fracture and flow properties were to the flow of the invading phase causing faster
 136 or slower breakthrough of the invading phase. As an example, the time required to complete the different
 137 simulations for different capillary numbers is shown in Figure S1.
 138

139 2.2 Description of simulation cases

140 Table 1 summarizes the different fracture and flow parameters considered in this work. For the fracture
 141 parameters, Hurst exponent and rms roughness were considered. We considered these for three fracture seeds.
 142 For flow parameters, we considered contact angles (reported against the defending phase), capillary numbers
 143 ($N_{ca} = \mu_i U / \sigma$) and viscosity ratio ($M = \mu_i / \mu_d$), where U is the Darcy velocity, σ is the fluid-fluid interfacial
 144 tension, and μ_i and μ_d are the viscosities of the invading and defending phases, respectively. All parameter
 145 ranges were tested thoroughly to arrive at these numbers to prevent numerical instabilities that could occur
 146 with the LBM simulator under extreme values. We coupled the analysis of viscosity ratios together with
 147 capillary numbers to study different displacement regimes of the invading phase. With these cases, we were
 148 able to investigate a broad range of flow and fracture properties to study their impact on the dynamics of
 149 multiphase flow.

Table 1: Summary of the different fracture and flow parameters and their range tested in this research.

Parameter	Values tested	Units
Rms roughness	[1, 2, 3, 4, 5, 6]	[1]
Fracture seed	[1, 2, 3]	[-]
Hurst exponent	[0.1, 0.2, 0.3, 0.4, 0.5, 0.6, 0.7, 0.8, 0.9, 0.95]	[-]
Contact angle	[10, 30, 50, 70, 90, 110]	[°]
Capillary number	[5^{-1} , 1^{-1} , 5^{-2} , 1^{-2} , 5^{-3} , 1^{-3} , 5^{-4} , 1^{-4} , 5^{-5} , 1^{-5} , 5^{-6}]	[-]
Invading phase viscosity	[0.004, 0.04, 0.2]	LBM units
Receding phase viscosity	[0.004, 0.04]	LBM units
Viscosity ratio	[10.0, 1.0, 0.1, 0.02]	[-]

3 Results and discussion

3.1 Dynamics of multiphase flow through single fracture media

Figure 1 shows the breakthrough saturation (BTS) for different fracture and flow parameters. Here, we observe that as Hurst exponent decreases, the BTS decreases, showing that the displacement is relatively unstable whereas at larger Hurst exponents, the BTS values are larger (stable displacement) owing to less roughness. Note that at the largest value of Hurst exponent, breakthrough still occurred at a value less than one, owing to flow controlled by the rms roughness parameter. With larger rms roughness, the BTS is affected significantly. A nearly linear trend is observed here for the range of rms roughness tested.

It is useful to note that when setting simulations for the Hurst exponent (Figure 1a), surface roughness, contact angle, and capillary numbers were set to 4, 45° , and 10^{-4} , respectively. Similarly, for simulations to test surface roughness (Figure 1b), capillary number and contact angle were set as previously, while Hurst exponent was set at 0.7. For contact angle cases (Figure 1c), Hurst exponent, surface roughness, and capillary number were set at 0.7, 4, and 10^{-4} , respectively. Lastly, for the capillary number cases (Figure 1d), Hurst exponent, surface roughness, and contact angle were set at 0.7, 4, and 45° , respectively. In addition, the viscosity ratio between invading and receding phase was set at 1.0 throughout the cases discussed in Figure 1. The parameter values set here were arrived at after intensive testing to keep the fixed attributes in the middle of their respective ranges so as not to have their impact dominate flow.

From Figure 1c we find that wettability has a significant impact on the flow of fluids inside the fracture. At low contact angles, the invading phase is nonwetting to the medium and has an unstable displacement with BTS as low as 0.5, whereas when the invading phase is weakly- to neutral nonwetting, the front moves stably through the fracture. Similar findings for the effect of wettability have been shown through multiphase experiments in 2D microfluidic cell where compact displacement of the invading phase was observed around neutral wettability Zhao et al. (2016). Capillary number, similarly, shows a strong impact on fluid invasion through the fracture. As expected, lower capillary numbers led to more stable displacements and vice versa (Figure 1d). We provide a detailed analysis on the role of capillary number in Figure 2.

The right column in Figure 1 shows the progression of the invading front into the fracture plotted against the saturation of the invading phase for the different cases discussed in the left column of Figure 1. The length of the invading front is normalized against the entire length of the fracture (512 μm). For all properties tested, a range of behavior is observed from faster to slower progression of the invading front. The impact of local heterogeneity can be captured here through irregular movement of the invading front. Stable displacement falls near the $y = x$ line on the plot. Both Hurst exponent and rms roughness led to faster movement of

181 the invading front. Similarly, strong nonwetting behavior of the invading fluid as well as higher capillary
 182 numbers led to unstable displacement. For the Hurst exponent, the value of 0.7, marked a transition in the
 183 profile of the invading front. Similarly, stable displacement threshold for rms roughness was found at ≤ 3.0 .
 184 For contact angles, stable displacement threshold was found to be at $\geq 70^\circ$. Lastly, for capillary numbers,
 185 stable displacement threshold was found to be at 10^{-3} . The step-like nature of the front progression reveals
 186 the presence of capillary fingering Tsuji et al. (2016), Bakhshian et al. (2019), visible for cases with Hurst
 187 exponent, rms roughness ≥ 3.0 , and contact angle $\geq 50^\circ$, while viscous fingering was observed for capillary
 188 number $\geq 5 \times 10^{-3}$.

189 Overall, BTS values are not observed to be below 0.5 in all cases tested here. We find that cases with
 190 Hurst exponent shows larger variance with the fracture seed and less variation in the BTS values [$\approx 0.65-0.8$]
 191 across the different Hurst exponent. Comparatively, other properties show at least a 0.3-unit difference in the
 192 observed BTS values. This suggests that Hurst exponent as a parameter has less effect on the displacement
 193 regime of the invading fluid. Particularly, the impact of contact angle and rms roughness is the most evident
 194 and their effect is explored in more detail in the following sections.

195 3.2 Displacement patterns across a single complex fracture

196 Figure 2 shows the breakthrough saturation and invading fluid progression through the exact same fracture for
 197 different viscosity ratios and capillary numbers. In developing this fracture realization rms roughness and Hurst
 198 exponent, were fixed at 4 and 0.7, respectively, while the seed was set at one. In addition, for these simulations,
 199 contact angle was set to 45° . Only viscosity ratios (10.0, 1.0, 0.1, and 0.02) and capillary numbers (ranging
 200 from 5×10^{-2} to 5×10^{-6}) were varied. Note that for viscosity ratios of 0.1 and 0.02, at very high capillary
 201 numbers of 5×10^{-2} , simulations failed to complete till the breakthrough point due to velocity-caused numerical
 202 instabilities in the simulator and, therefore, these data points are not available for comparison. Nevertheless,
 203 the wide range of capillary numbers tested provide meaningful data to make useful comparisons.

204 From Figure 2a, it is observed that the behavior of flow is highly dependent on the flow conditions. For
 205 higher viscosity ratio (10.0), the flow of invading phase is stable and the BTS is less impacted by capillary
 206 number, meaning regardless of the input velocity change, the invading front progresses through the fracture
 207 remained the same (Figure 2b), where the fronts fall near the $y=x$ line. For the viscosity ratio of one (Figure 2a
 208 blue curve), invading phase is dependent on the capillary number. This was previously discussed in Section 3.1.
 209 (Figure 1d). Finally, for the lower viscosity ratios (0.1 and 0.02), where the invading phase is less viscous, the
 210 dependence of the movement of the invading phase on flow velocity is further enhanced. The BTS values for
 211 this case change significantly ranging from $\approx 0.42-0.85$. A steep linear dependence is found between capillary
 212 number on the log-scale and BTS. Viscosity ratio of 1.0 is found to be a transition case where both constant
 213 BTS and linear changes in BTS with capillary number is found. For viscosity ratios ≤ 1.0 , higher capillary
 214 number led to faster breakthroughs, while lower capillary numbers, the movement of front becomes more stable
 215 (Fig. S2 c, d and e) leading to larger BTS values. At the limit of very low capillary numbers, the dependence
 216 on viscosity ratios minimizes and BTS is controlled by the inherent fracture property (input of rms roughness).

217 We develop a phase diagram in Figure 2b to describe different displacement regimes from the data in
 218 Figure 2a. It is conceptualized through a contour map of BTS values of the invading phase to assess the
 219 stability of a displacement regime. The faster the BTS, more unstable the displacement and vice versa. This
 220 is plotted on a mesh of capillary numbers and viscosity ratios similar to the experimental work of Chen et al.

221 (2017), Chen, Wu, Fang & Hu (2018). The data points that were unavailable due to numerical instabilities
 222 were set to the last available data point. With viscosity ratios between 0.02 to 10, we focus in the transition
 223 zone between viscous and capillary regimes as seen from the traditional Lenormand diagram Lenormand
 224 et al. (1988), Lenormand & Zarcone (1984) that was developed through simplified pore-network experiments
 225 Lenormand et al. (1983). One reason is that the transition zone is not well explored in the literature, especially
 226 for flow through complex fractures and also that these viscosity ratios (0.1 and 0.02) are relevant for physical
 227 systems representative of CO₂-water as well as H₂-water injection for the purposes of geological gas storage
 228 Herring et al. (2016), Chen et al. (2019), Delshad et al. (2022). We find that lower capillary numbers result
 229 in stability of flow for all viscosity ratios. At larger capillary numbers, however, the stability is strongly
 230 dependent on viscosity ratios, moving from the most unstable at low viscosity ratios to the most stable at high
 231 viscosity ratios. At viscosity ratio of 10.0, the flow is stable across most capillary numbers, with a slightly
 232 more stable zone around intermediate capillary numbers because around that zone, flow is controlled by the
 233 geometry of the flow domain dependent on the fracture properties. On the contrary, at low viscosity ratios,
 234 flow is mostly unstable across all capillary numbers, but becomes increasingly unstable as capillary numbers
 235 increases. Overall, the most unstable zone is found at high capillary numbers and low viscosity ratios, while
 236 the most stable zone is found at high viscosity ratios and intermediate capillary numbers. We overlay the
 237 boundaries of capillary fingering (bounded by the viscosity ratio axis), viscous fingering (bounded by the
 238 capillary number axis), and stable displacement (top-right corner) for traditional porous media Lenormand
 239 et al. (1988), Zhang et al. (2011) and for a single rough fracture Chen, Wu, Fang & Hu (2018). We find that in
 240 a single rough fracture the change in BTS values is significant ranging from ≈ 0.3 to 0.9 even when operating
 241 in the transition zone of the different displacement regimes making the boundary definition from Lenormand
 242 et al. (1988) less applicable. However, the boundaries as described in Zhang et al. (2011), Chen, Wu, Fang &
 243 Hu (2018) show a narrower representation of the transition zone slightly more representative of the observation
 244 from our simulations. In the next section, we extend this discussion across multiple rough fractures.

245 3.3 Displacement patterns across multiple complex fractures

246 In Figure 3 we describe displacement phase diagrams across different complex fractures whose rms roughness
 247 (2, 4, and 6) and wettability (30°, 50°, and 70°) are varied. Additional information for these fracture surface
 248 properties and corresponding dimensionless roughness parameters are given in Table S1 and the simulation
 249 data used to construct the phase diagrams are shown in Figure S3. As phase becomes more nonwetting,
 250 keeping viscosity ratios fixed, a delayed breakthrough is observed. Similarly, as the fracture becomes rough,
 251 there is a significant impact on BTS. At low roughness, the effect of capillary number is observed for viscosity
 252 ratios of 0.1 and 0.02. Even here for low capillary numbers, lower than 10^{-4} , leads to almost stable flow with
 253 much delayed breakthroughs (black contour line). The worst case is observed for $\theta = 30^\circ$ and roughness of 6,
 254 where breakthroughs range between 0.3 and 0.7. Effect of capillary number is seen more clearly for the case of
 255 roughness of 4 when viscosity ratios are 0.02 and 0.1. Here, nearly linear trend is seen with capillary number
 256 on log-scale (Figure S3) and the slope of the linear trend is found to be a dependent on wettability. Similarly,
 257 effect of wettability is found to be significant when roughness is 6. Despite such high roughness, for viscosity
 258 ratio of 10.0 and contact angle of 70°, BTS values are > 0.9 , showing stable displacement. In addition, all
 259 phase diagrams convey that at very low capillary number, the BTS tend to converge to a single value. This
 260 value can be as high as 1.0 (low rms roughness and high contact angle) to ≈ 0.5 (high rms roughness and low

261 contact angle) reinforcing that the inherent characteristic of the fracture ultimately govern the nature of fluid
262 invasion through the fracture.

263 Phase diagrams for very low viscosity ratios were developed for wettability against capillary number (Lan
264 et al. (2020)) and between roughness and capillary number (Hu et al. (2019)) through experiments, simulations,
265 and theoretical models. Our trends show general agreement such that the more nonwetting and the lower the
266 capillary number, more stable the displacement front; and that more smooth the fracture and the lower the
267 capillary number, more stable the displacement. In addition, these trends persists for most viscosity ratio,
268 however, the evolution of the stability of the displacement regime is found to be a function of all contributing
269 parameters: roughness, wettability, viscosity ratios, and capillary number. This helps us appreciate that such
270 displacement regimes can be significantly different from one fracture to another and that such generalizations
271 should be made with caution. This is for the first time that a representation of phase volume (instead of
272 traditional phase diagrams) delineating stable versus unstable displacement for flow through complex fractures
273 has been presented. In our future work, we will extend the analysis to quantify transport through averaged
274 properties such as permeability and relative permeability.

275 4 Conclusions

276 In this letter, we describe direct numerical multiphase simulations in different single fracture realizations to
277 study the impact of various fracture and flow parameters on the dynamics of invading fluid flow. For fracture
278 parameters, we vary the fracture seed and fracture roughness by varying the Hurst exponent and the rms
279 roughness parameter. For the flow, we test the effect of fracture wettability, capillary number, and viscosity
280 ratio. The simulations were performed using a high-fidelity physics-based lattice Boltzmann simulator. The
281 following conclusions are drawn:

282

- 283 • Hurst exponent, rms roughness, and wettability influence the dynamics of the invading phase flow through
284 the fracture. At low rms roughness, the invading phase migrates through the fracture in a piston-
285 like fashion while at larger values, sharper breakthroughs (≈ 0.6) are observed. For strong nonwetting
286 conditions (contact angle 10°), the invading phase breaks through at ≈ 0.5 saturation, while at neutral
287 wettability, the invading phase flows as a piston-like regime.
- 288 • For a single rough fracture, at low capillary numbers, the invading phase moves such that the BTS
289 is constrained by the fracture properties, regardless of the viscosity ratio. At high capillary numbers,
290 however, viscosity ratios significantly affect the movement of the invading phase when the viscosity ratio
291 are equal or unfavorable.
- 292 • Fluid displacement phase diagrams show that the viscosity ratios considered here fall within the cross-over
293 zone of the traditional Lenormand-type phase diagram and even within the cross-over zone, displacement
294 patterns are quite different when roughness and wettability attributes are varied. We demonstrate that
295 flow in fractured media cannot be described by a single flow regime phase diagram and is instead specific
296 to the fracture and flow conditions considered. Unlike traditional phase diagrams, a phase volume across
297 fracture roughness and wettability is developed to describe stable versus unstable displacement regimes
298 for multiphase flow through complex fractures.

299 **Nomenclature**

300	χ	Normalized front tip length
301	μ <i>CT</i>	Microcomputed tomography
302	μ_d	Defending fluid viscosity
303	μ_i	Invading fluid viscosity
304	σ	Fluid-fluid interfacial tension
305	θ	Contact angle measured through the receding phase
306	<i>BTS</i>	Breakthrough saturation
307	<i>LBM</i>	Lattice Boltzmann method
308	<i>lu</i>	Lattice unit
309	<i>M</i>	Viscosity ratio
310	<i>Nca</i>	Capillary number
311	<i>U</i>	Darcy velocity

312 **Data Availability Statement**

313 All of the data discussed in the paper is archived and available at <https://zenodo.org/record/8247637>.

314 **Software Availability Statement**

315 Synthetic fractures were generated using the pySimFrac toolkit available at [https://github.com/lanl/dfnWorks/](https://github.com/lanl/dfnWorks/tree/pysimfrac/pysimfrac)
316 [tree/pysimfrac/pysimfrac](https://github.com/lanl/dfnWorks/tree/pysimfrac/pysimfrac) Gultinan et al. (2023). The multiphase simulations in this research were per-
317 formed using the MF-LBM code available at <https://github.com/lanl/mf-lbm> Chen et al. (2019) distributed
318 under the BSD-3 license. The extracted data from the simulation presented in this research was processed using
319 1) MS-Excel (version 2306) for data analysis and generating simple plots; 2) ParaView for the visualization of
320 the front movement (ParaView version 5.11.0) available at <https://www.paraview.org/> Ahrens et al. (2005),
321 Ayachit (2015); and 3) matplotlib for plotting the breakthrough saturation contour plots in the paper available
322 at <https://matplotlib.org/>.

323 **Acknowledgement**

324 Research presented in this article was supported by the Laboratory Directed Research and Development pro-
325 gram of Los Alamos National Laboratory under project number XXKF00 & XXFT00 and has been designated
326 with the Los Alamos Unlimited Release number LA-UR-23-29351. J.E.S. would like to thank the Center for
327 Nonlinear Studies for support. J.D.H. acknowledges support from the Department of Energy (DOE) Basic
328 Energy Sciences program (LANLE3W1) for support. The research was supported as part of the Center on
329 Geo-process in Mineral Carbon Storage, an Energy Frontier Research Center funded by the U.S. Department

330 of Energy (DOE), Office of Science, Basic Energy Sciences (BES), under award # DE-SC0023429. This work
331 has been partially funded by the Spent Fuel and Waste Science and Technology (SFWST) Campaign of the
332 U.S. Department of Energy Office of Nuclear Energy. The views expressed in the article do not necessarily
333 represent the views of the U.S. Department of Energy or the United States Government.

334

335 References

- 336 1. Ahrens, J. P., Geveci, B. & Law, C. C. (2005), Paraview: An end-user tool for large-data visualization,
337 in ‘The Visualization Handbook’.
338 **URL:** <https://api.semanticscholar.org/CorpusID:56558637>
- 339 2. Akai, T., Bijeljic, B. & Blunt, M. J. (2018), ‘Wetting boundary condition for the color-gradient lattice
340 boltzmann method: Validation with analytical and experimental data’, *Advances in Water Resources*
341 **116**, 56–66.
342 **URL:** <https://www.sciencedirect.com/science/article/pii/S030917081731028X>
- 343 3. Ayachit, U. (2015), *The ParaView Guide: A Parallel Visualization Application*, Kitware, Inc., Clifton
344 Park, NY, USA.
- 345 4. Babadagli, T., Raza, S., Ren, X. & Develi, K. (2015), ‘Effect of surface roughness and lithology on the
346 water–gas and water–oil relative permeability ratios of oil-wet single fractures’, *International Journal*
347 *of Multiphase Flow* **75**, 68–81.
348 **URL:** <https://www.sciencedirect.com/science/article/pii/S0301932215001226>
- 349 5. Bakhshian, S., Hosseini, S. A. & Shokri, N. (2019), ‘Pore-scale characteristics of multiphase flow in
350 heterogeneous porous media using the lattice boltzmann method’, *Scientific Reports* **9**(1), 1–13.
351 **URL:** <https://doi.org/10.1038/s41598-019-39741-x>
- 352 6. Bertels, S. P., DiCarlo, D. A. & Blunt, M. J. (2001), ‘Measurement of aperture distribution, capillary
353 pressure, relative permeability, and in situ saturation in a rock fracture using computed tomography
354 scanning’, *Water Resources Research* **37**(3), 649–662.
355 **URL:** <https://agupubs.onlinelibrary.wiley.com/doi/abs/10.1029/2000WR900316>
- 356 7. Birkholzer, J., Houseworth, J. & Tsang, C.-F. (2012), ‘Geologic disposal of high-level radioactive waste:
357 Status, key issues, and trends’, *Annual Review of Environment and Resources* **37**(1), 79–106.
358 **URL:** <https://doi.org/10.1146/annurev-environ-090611-143314>
- 359 8. Brackbill, J., Kothe, D. & Zemach, C. (1992), ‘A continuum method for modeling surface tension’,
360 *Journal of Computational Physics* **100**(2), 335–354.
361 **URL:** <https://www.sciencedirect.com/science/article/pii/002199919290240Y>
- 362 9. Brown, S. R. (1995), ‘Simple mathematical model of a rough fracture’, *Journal of Geophysical Research:*
363 *Solid Earth* **100**(B4), 5941–5952.
364 **URL:** <https://agupubs.onlinelibrary.wiley.com/doi/abs/10.1029/94JB03262>

- 365 10. Chen, Y.-F., Fang, S., Wu, D.-S. & Hu, R. (2017), ‘Visualizing and quantifying the crossover from
366 capillary fingering to viscous fingering in a rough fracture’, *Water Resources Research* **53**(9), 7756–
367 7772.
368 **URL:** <https://agupubs.onlinelibrary.wiley.com/doi/abs/10.1002/2017WR021051>
- 369 11. Chen, Y.-F., Wu, D.-S., Fang, S. & Hu, R. (2018), ‘Experimental study on two-phase flow in rough
370 fracture: Phase diagram and localized flow channel’, *International Journal of Heat and Mass Transfer*
371 **122**, 1298–1307.
372 **URL:** <https://www.sciencedirect.com/science/article/pii/S0017931017354832>
- 373 12. Chen, Y., Li, Y., Valocchi, A. J. & Christensen, K. T. (2018), ‘Lattice boltzmann simulations of liquid
374 co2 displacing water in a 2d heterogeneous micromodel at reservoir pressure conditions’, *Journal of*
375 *Contaminant Hydrology* **212**, 14–27.
376 **URL:** <https://www.sciencedirect.com/science/article/pii/S0169772217300645>
- 377 13. Chen, Y., Valocchi, A. J., Kang, Q. & Viswanathan, H. S. (2019), ‘Inertial effects during the pro-
378 cess of supercritical co2 displacing brine in a sandstone: Lattice boltzmann simulations based on the
379 continuum-surface-force and geometrical wetting models’, *Water Resources Research* **55**(12), 11144–
380 11165.
381 **URL:** <https://agupubs.onlinelibrary.wiley.com/doi/abs/10.1029/2019WR025746>
- 382 14. Culligan, K. A., Wildenschild, D., Christensen, B. S. B., Gray, W. G., Rivers, M. L. & Tompson, A.
383 F. B. (2004), ‘Interfacial area measurements for unsaturated flow through a porous medium’, *Water*
384 *Resources Research* **40**(12).
385 **URL:** <https://agupubs.onlinelibrary.wiley.com/doi/abs/10.1029/2004WR003278>
- 386 15. Culligan, K., Wildenschild, D., Christensen, B., Gray, W. & Rivers, M. (2006), ‘Pore-scale charac-
387 teristics of multiphase flow in porous media: A comparison of air–water and oil–water experiments’,
388 *Advances in Water Resources* **29**(2), 227–238. Experimental Hydrology: A Bright Future.
389 **URL:** <https://www.sciencedirect.com/science/article/pii/S030917080500120X>
- 390 16. Delshad, M., Umurzakov, Y., Sepehrnoori, K., Eichhubl, P. & Batista Fernandes, B. R. (2022), ‘Hy-
391 drogen storage assessment in depleted oil reservoir and saline aquifer’, *Energies* **15**(21).
392 **URL:** <https://www.mdpi.com/1996-1073/15/21/8132>
- 393 17. d’Humières, D., Ginzburg, I., Krafczyk, M., Lallemand, P. & Luo, L.-S. (2002), ‘Multiple-relaxation-
394 time lattice boltzmann models in three dimensions’, *Philosophical Transactions of the Royal Society of*
395 *London. Series A: Mathematical, Physical and Engineering Sciences* **360**(1792), 437–451.
396 **URL:** <https://royalsocietypublishing.org/doi/abs/10.1098/rsta.2001.0955>
- 397 18. Dou, Z., Zhou, Z. & Sleep, B. (2013), ‘Influence of wettability on interfacial area during immiscible
398 liquid invasion into a 3d self-affine rough fracture: Lattice boltzmann simulations’, *Advances in Water*
399 *Resources* **61**, 1–11.
400 **URL:** <https://www.sciencedirect.com/science/article/pii/S0309170813001462>

- 401 19. Gale, J. F. W., Reed, R. M. & Holder, J. (2007), ‘Natural fractures in the Barnett Shale and their
402 importance for hydraulic fracture treatments’, *AAPG Bulletin* **91**(4), 603–622.
403 **URL:** <https://doi.org/10.1306/11010606061>
- 404 20. Ghanbarzadeh, S., Hesse, M. A., Prodanović, M. & Gardner, J. E. (2015), ‘Deformation-assisted fluid
405 percolation in rock salt’, *Science* **350**(6264), 1069–1072.
406 **URL:** <https://www.science.org/doi/abs/10.1126/science.aac8747>
- 407 21. Glover, P., Matsuki, K., Hikima, R. & Hayashi, K. (1998a), ‘Fluid flow in synthetic rough fractures
408 and application to the hachimantai geothermal hot dry rock test site’, *Journal of Geophysical Research:*
409 *Solid Earth* **103**(B5), 9621–9635.
- 410 22. Glover, P., Matsuki, K., Hikima, R. & Hayashi, K. (1998b), ‘Synthetic rough fractures in rocks’, *Journal*
411 *of Geophysical Research: Solid Earth* **103**(B5), 9609–9620.
- 412 23. Glover, P., Matsuki, K., Hikima, R. & Hayashi, K. (1999), ‘Characterizing rock fractures using synthetic
413 fractal analogues’, *Geothermal science and technology* **6**(1-4), 83–112.
- 414 24. Guiltinan, E. J., Santos, J. E., Cardenas, M. B., Espinoza, D. N. & Kang, Q. (2021), ‘Two-phase
415 fluid flow properties of rough fractures with heterogeneous wettability: Analysis with lattice boltzmann
416 simulations’, *Water Resources Research* **57**(1), e2020WR027943.
417 **URL:** <https://agupubs.onlinelibrary.wiley.com/doi/abs/10.1029/2020WR027943>
- 418 25. Guiltinan, E. J., Santos, J. E., Purswani, P. & Hyman, J. D. (2023), ‘Pysimfrac: A python library for
419 synthetic fracture generation, analysis, and simulation’, *Computers & Geosciences* **Submitted**.
- 420 26. Herring, A. L., Andersson, L. & Wildenschild, D. (2016), ‘Enhancing residual trapping of supercritical
421 co2 via cyclic injections’, *Geophysical Research Letters* **43**(18), 9677–9685.
422 **URL:** <https://agupubs.onlinelibrary.wiley.com/doi/abs/10.1002/2016GL070304>
- 423 27. Hu, R., Zhou, C.-X., Wu, D.-S., Yang, Z. & Chen, Y.-F. (2019), ‘Roughness control on multiphase flow
424 in rock fractures’, *Geophysical Research Letters* **46**(21), 12002–12011.
425 **URL:** <https://agupubs.onlinelibrary.wiley.com/doi/abs/10.1029/2019GL084762>
- 426 28. Hussain, S. T., Rahman, S. S., Azim, R. A., Haryono, D. & Regenauer-Lieb, K. (2021), ‘Multiphase
427 fluid flow through fractured porous media supported by innovative laboratory and numerical methods
428 for estimating relative permeability’, *Energy & Fuels* **35**(21), 17372–17388.
429 **URL:** <https://doi.org/10.1021/acs.energyfuels.1c01313>
- 430 29. Hyman, J. D., Karra, S., Makedonska, N., Gable, C. W., Painter, S. L. & Viswanathan, H. S. (2015),
431 ‘dfnworks: A discrete fracture network framework for modeling subsurface flow and transport’, *Com-*
432 *puters Geosciences* **84**, 10–19.
433 **URL:** <https://www.sciencedirect.com/science/article/pii/S0098300415300261>
- 434 30. Hyman, J. D., Sweeney, M. R., Frash, L. P., Carey, J. W. & Viswanathan, H. S. (2021), ‘Scale-bridging
435 in three-dimensional fracture networks: Characterizing the effects of variable fracture apertures on
436 network-scale flow channelization’, *Geophysical Research Letters* **48**(19), e2021GL094400.

- 437 31. Karpyn, Z., Grader, A. & Halleck, P. (2007), ‘Visualization of fluid occupancy in a rough fracture using
438 micro-tomography’, *Journal of Colloid and Interface Science* **307**(1), 181–187.
439 **URL:** <https://www.sciencedirect.com/science/article/pii/S0021979706010149>
- 440 32. Khosravi, M., Bahramian, A., Emadi, M., Rostami, B. & Roayaie, E. (2014), ‘Mechanistic investigation
441 of bypassed-oil recovery during co2 injection in matrix and fracture’, *Fuel* **117**, 43–49.
442 **URL:** <https://www.sciencedirect.com/science/article/pii/S0016236113009356>
- 443 33. Lan, T., Hu, R., Yang, Z., Wu, D.-S. & Chen, Y.-F. (2020), ‘Transitions of fluid invasion patterns in
444 porous media’, *Geophysical Research Letters* **47**(20), e2020GL089682. e2020GL089682 2020GL089682.
445 **URL:** <https://agupubs.onlinelibrary.wiley.com/doi/abs/10.1029/2020GL089682>
- 446 34. Landry, C. J., Karpyn, Z. T. & Ayala, O. (2014), ‘Relative permeability of homogenous-wet and mixed-
447 wet porous media as determined by pore-scale lattice boltzmann modeling’, *Water Resources Research*
448 **50**(5), 3672–3689.
449 **URL:** <https://agupubs.onlinelibrary.wiley.com/doi/abs/10.1002/2013WR015148>
- 450 35. Leclaire, S., Abahri, K., Belarbi, R. & Bennacer, R. (2016), ‘Modeling of static contact angles with
451 curved boundaries using a multiphase lattice boltzmann method with variable density and viscosity
452 ratios’, *International Journal for Numerical Methods in Fluids* **82**(8), 451–470.
453 **URL:** <https://onlinelibrary.wiley.com/doi/abs/10.1002/fld.4226>
- 454 36. Leclaire, S., Parmigiani, A., Malaspinas, O., Chopard, B. & Latt, J. (2017), ‘Generalized three-
455 dimensional lattice boltzmann color-gradient method for immiscible two-phase pore-scale imbibition
456 and drainage in porous media’, *Phys. Rev. E* **95**, 033306.
457 **URL:** <https://link.aps.org/doi/10.1103/PhysRevE.95.033306>
- 458 37. Lenormand, R., Touboul, E. & Zarcone, C. (1988), ‘Numerical models and experiments on immiscible
459 displacements in porous media’, *Journal of Fluid Mechanics* **189**, 165–187.
- 460 38. Lenormand, R. & Zarcone, C. (1984), ‘Role Of Roughness And Edges During Imbibition In Square
461 Capillaries’, pp. SPE-13264-MS.
462 **URL:** <https://doi.org/10.2118/13264-MS>
- 463 39. Lenormand, R., Zarcone, C. & Sarr, A. (1983), ‘Mechanisms of the displacement of one fluid by another
464 in a network of capillary ducts’, *Journal of Fluid Mechanics* **135**, 337–353.
- 465 40. March, R., Doster, F. & Geiger, S. (2018), ‘Assessment of co2 storage potential in naturally fractured
466 reservoirs with dual-porosity models’, *Water Resources Research* **54**(3), 1650–1668.
467 **URL:** <https://agupubs.onlinelibrary.wiley.com/doi/abs/10.1002/2017WR022159>
- 468 41. McClure, J. E., Armstrong, R. T., Berrill, M. A., Schlüter, S., Berg, S., Gray, W. G. & Miller, C. T.
469 (2018), ‘Geometric state function for two-fluid flow in porous media’, *Phys. Rev. Fluids* **3**, 084306.
470 **URL:** <https://link.aps.org/doi/10.1103/PhysRevFluids.3.084306>
- 471 42. Ogilvie, S. R., Isakov, E. & Glover, P. W. (2006), ‘Fluid flow through rough fractures in rocks. ii: A
472 new matching model for rough rock fractures’, *Earth and Planetary Science Letters* **241**(3), 454–465.
473 **URL:** <https://www.sciencedirect.com/science/article/pii/S0012821X05008174>

- 474 43. Primkulov, B. K., Pahlavan, A. A., Fu, X., Zhao, B., MacMinn, C. W. & Juanes, R. (2019), ‘Signatures
475 of fluid–fluid displacement in porous media: wettability, patterns and pressures’, *Journal of Fluid*
476 *Mechanics* **875**, R4.
- 477 44. Primkulov, B. K., Pahlavan, A. A., Fu, X., Zhao, B., MacMinn, C. W. & Juanes, R. (2021), ‘Wettability
478 and lenormand’s diagram’, *Journal of Fluid Mechanics* **923**, A34.
- 479 45. Reeves, P. C. & Celia, M. A. (1996), ‘A functional relationship between capillary pressure, saturation,
480 and interfacial area as revealed by a pore-scale network model’, *Water Resources Research* **32**(8), 2345–
481 2358.
482 **URL:** <https://agupubs.onlinelibrary.wiley.com/doi/abs/10.1029/96WR01105>
- 483 46. Song, W., Prodanovic, M., Santos, J. E., Yao, J., Zhang, K. & Yang, Y. (2023), ‘Upscaling of Transport
484 Properties in Complex Hydraulic Fracture Systems’, *SPE Journal* **28**(03), 1026–1044.
485 **URL:** <https://doi.org/10.2118/212849-PA>
- 486 47. Tsuji, T., Jiang, F. & Christensen, K. T. (2016), ‘Characterization of immiscible fluid displacement
487 processes with various capillary numbers and viscosity ratios in 3d natural sandstone’, *Advances in*
488 *Water Resources* **95**, 3–15. Pore scale modeling and experiments.
489 **URL:** <https://www.sciencedirect.com/science/article/pii/S0309170816300550>
- 490 48. Wang, Y., Vuik, C. & Hajibeygi, H. (2022), ‘Co2 storage in deep saline aquifers: impacts of fractures
491 on hydrodynamic trapping’, *International Journal of Greenhouse Gas Control* **113**, 103552.
492 **URL:** <https://www.sciencedirect.com/science/article/pii/S1750583621003030>
- 493 49. Xu, Z., Liu, H. & Valocchi, A. J. (2017), ‘Lattice boltzmann simulation of immiscible two-phase flow
494 with capillary valve effect in porous media’, *Water Resources Research* **53**(5), 3770–3790.
495 **URL:** <https://agupubs.onlinelibrary.wiley.com/doi/abs/10.1002/2017WR020373>
- 496 50. Yi, J., Xing, H., Wang, J., Xia, Z. & Jing, Y. (2019), ‘Pore-scale study of the effects of surface rough-
497 ness on relative permeability of rock fractures using lattice boltzmann method’, *Chemical Engineering*
498 *Science* **209**, 115178.
499 **URL:** <https://www.sciencedirect.com/science/article/pii/S0009250919306694>
- 500 51. Zhang, C., Oostrom, M., Wietsma, T. W., Grate, J. W. & Warner, M. G. (2011), ‘Influence of viscous
501 and capillary forces on immiscible fluid displacement: Pore-scale experimental study in a water-wet
502 micromodel demonstrating viscous and capillary fingering’, *Energy & Fuels* **25**(8), 3493–3505.
503 **URL:** <https://doi.org/10.1021/ef101732k>
- 504 52. Zhao, B., MacMinn, C. W. & Juanes, R. (2016), ‘Wettability control on multiphase flow in patterned
505 microfluidics’, *Proceedings of the National Academy of Sciences* **113**(37), 10251–10256.
506 **URL:** <https://www.pnas.org/doi/abs/10.1073/pnas.1603387113>
- 507 53. Zhou, C.-B., Chen, Y.-F., Hu, R. & Yang, Z. (2023), ‘Groundwater flow through fractured rocks and
508 seepage control in geotechnical engineering: Theories and practices’, *Journal of Rock Mechanics and*
509 *Geotechnical Engineering* **15**(1), 1–36.
510 **URL:** <https://www.sciencedirect.com/science/article/pii/S1674775522002013>

511 **List of Figures**

512 1 Breakthrough saturation and front migration profiles for different fracture and flow
513 parameters. All data points reported for the BTS values are average of three seeds
514 used for generating fracture realizations and standard deviation is estimated from this
515 triplicate information. For tracking the front migration, normalized front tip length (χ)
516 is obtained for the front tip length at any given saturation divided by the total number
517 of lus in the direction of flow (512 lus for all fractures considered in this work). Here,
518 the normalized front tip lengths are shown only for seed 1. 16

519 2 (a) Breakthrough saturation for different viscosity ratios and capillary numbers. (b)
520 Phase diagram showing different displacement regimes in the same fracture realization.
521 Boundaries for viscous fingering, capillary fingering, and stable displacement from the
522 Lenormand and Lenormand-type diagrams are overlain on the plot (Lenormand et al.
523 (1988), Zhang et al. (2011), Chen, Wu, Fang & Hu (2018). The region bounded in the
524 top-right corresponds to stable displacement while the region bounded by the viscosity
525 ratio axis corresponds to capillary fingering. Similarly, the region bounded by the cap-
526 illary number axis corresponds to the viscous fingering. The following fracture and flow
527 properties were fixed in these figures rms roughness = 4, Hurst exponent = 0.7, seed =
528 1, and contact angle = 45° 17

529 3 Displacement pattern phase diagrams for different fractures. Three different rms rough-
530 ness values (2, 4, and 6) and three different contact angle cases (30° , 50° , and 70°) are
531 considered for the full range of capillary numbers and viscosity ratios discussed pre-
532 viously in Figure 2b. All simulations discussed here are for seed one and the Hurst
533 exponent was fixed at 0.7. 18

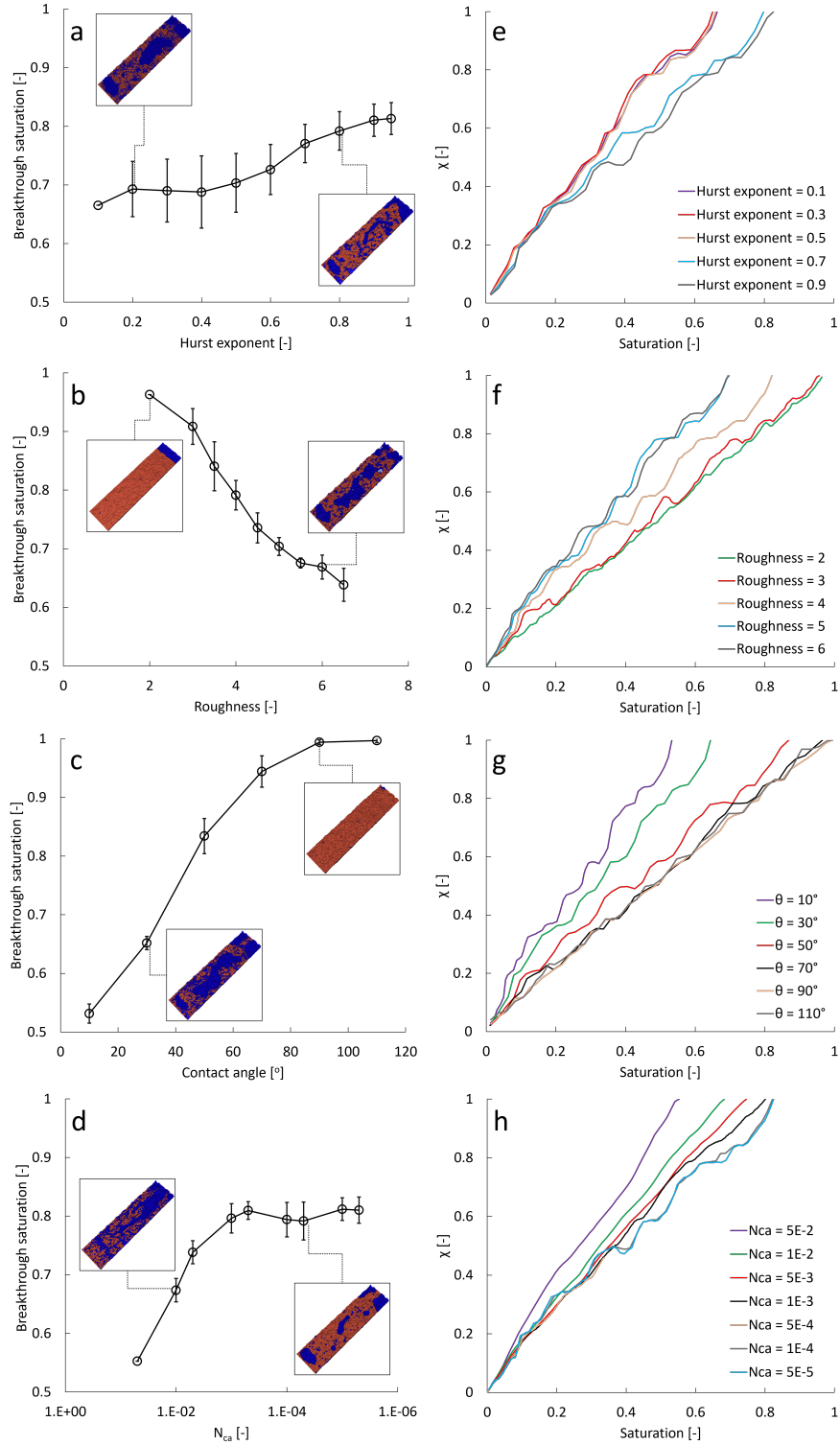


Figure 1: Breakthrough saturation and front migration profiles for different fracture and flow parameters. All data points reported for the BTS values are average of three seeds used for generating fracture realizations and standard deviation is estimated from this triplicate information. For tracking the front migration, normalized front tip length (χ) is obtained for the front tip length at any given saturation divided by the total number of lus in the direction of flow (512 lus for all fractures considered in this work). Here, the normalized front tip lengths are shown only for seed 1.

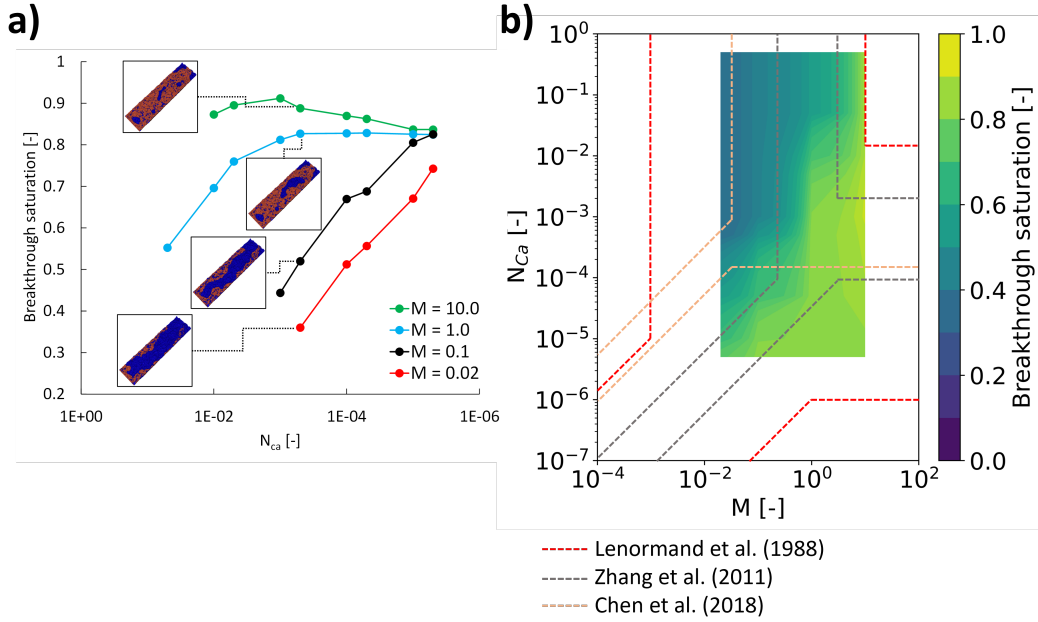


Figure 2: (a) Breakthrough saturation for different viscosity ratios and capillary numbers. (b) Phase diagram showing different displacement regimes in the same fracture realization. Boundaries for viscous fingering, capillary fingering, and stable displacement from the Lenormand and Lenormand-type diagrams are overlain on the plot (Lenormand et al. (1988), Zhang et al. (2011), Chen, Wu, Fang & Hu (2018)). The region bounded in the top-right corresponds to stable displacement while the region bounded by the viscosity ratio axis corresponds to capillary fingering. Similarly, the region bounded by the capillary number axis corresponds to the viscous fingering. The following fracture and flow properties were fixed in these figures rms roughness = 4, Hurst exponent = 0.7, seed = 1, and contact angle = 45° .

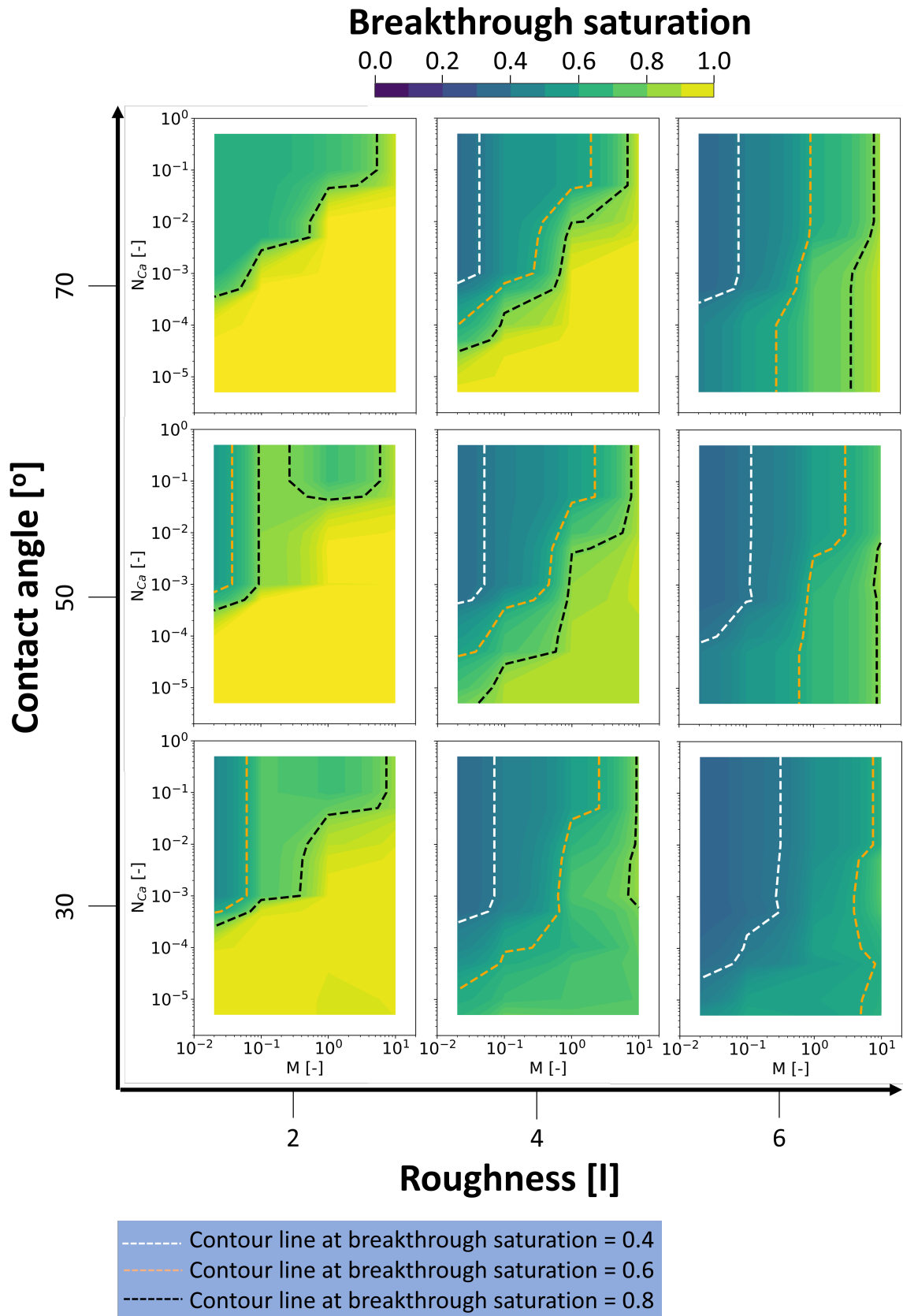


Figure 3: Displacement pattern phase diagrams for different fractures. Three different rms roughness values (2, 4, and 6) and three different contact angle cases (30°, 50°, and 70°) are considered for the full range of capillary numbers and viscosity ratios discussed previously in Figure 2b. All simulations discussed here are for seed one and the Hurst exponent was fixed at 0.7.